# 5

# CHARACTERISATION OF THE GROWN CRYSTALS

## 5.1 Introduction

The characterisation of the crystals is an important component of the study of crystals. This helps the crystal grower to assess the quality, nature and property of the crystals. A large number of experimental techniques exist to assess the composition, quality and the presence of its constituent elements. The experimental methods used to characterise crystals include surface microphotography, spectroscopic analysis, thermogravimetric analysis etc. This chapter describes the characterisation of the grown rare earth hydrogen selenite crystals in detail.

## 5.2 Surface study of crystals

The properties of solid state materials including crystals are mainly based on its micro and macro structures. The dependence of the properties on the microstructure is generally very complicated and unravelling it is really a herculean task for the investigators. The lattice structure and the associated lattice defects play a major role

in determining the properties of the crystals. Several experimental techniques complimenting one another are used for the detection of the lattice defects and other parameters. The study of the surface of the crystal gives valuable information about its internal structure.

The defects on the surface of the materials have a characteristic role on the growth and morphology of the crystals. The surface by itself is actually a lattice defect as it is the abrupt termination of the periodic lattice. The basic problem is inherent to the surface of solid materials. It is due to the fact that the surface atoms are chemically unsaturated. Therefore it has an inherent tendency to react physically and or chemically with its surroundings and this may lead to contamination or corrosion. Hence it is expected that the study of the surface in detail will throw light on the characteristics of the bulk material.

### 5.2.1 Morphology of the rare earth hydrogen selenite crystals

Laboratory grown crystal shows different types of morphologies (fig.5.1). In the same condition of growth, mono and mixed hydrogen selenite crystals show same type of morphology but it varies with growth conditions. The morphological changes observed are a result of the changes in different gel parameters and concentration of the reactants.

The observed morphology[1] at different conditions are

1. Epidote, prismatic in the direction of ortho-axis layered crystals
2. Rectangular (diametral prism) layered crystals
3. Twinned crystals
4. Spherulitic and dendrite crystals

All the grown rare earth hydrogen selenite crystals (mono and mixed) are thin prismatic and of longer dimension in the direction of the ortho-axis. The growths of the surface of the crystals are in the form of layers. The most developed faces [100] of these crystals are layered and shining (fig. 5.2 (f)). It is observed that the crystals found at the bottom of the gel column are well faceted and transparent. On the other

hand the crystals at the gel solution interface are more defective. Twinned crystals are invariably seen in large numbers near the gel solution interface and they are of lesser perfection. The layered nature of the crystals is due to the higher supersaturation conditions, but they are less perfect. This is evident especially in the case of samarium hydrogen selenite and its mixed crystals. Due to the higher supersaturation the bunching of the crystals occur predominantly in the near surface of the gel column. Irregularities also occur due to the bunching or clustering of the crystals. The bunching is more predominant in the case of crystals containing praseodymium. Stoichiometric variations also cause the bunching in the case of mixed crystals.

A detailed study of the morphology of all the grown crystals show that the morphology like needle, dendrite etc. of the crystal whether mono or mixed depends mainly on the region in the crystalliser. Fig. 5.1 shows the different morphology of the crystals. Twinning and bunching are observed in all cases. As far as we know, this is the first time mixed rare earth hydrogen selenite crystals have been grown by gel method. The photographs (fig. 5.2 (a-e) show the morphologies of the grown crystals. Most of the crystals are prismatic, layered in nature and they have non-isometric shape. Twinning is one of the common habits of the grown crystals. The most prominent face of all these crystals are [100]

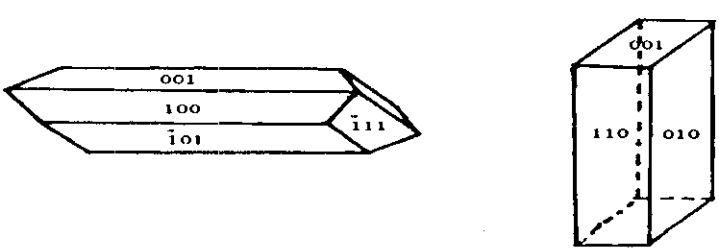


Fig. 5.1 Morphology of rare earth hydrogen selenite crystals

## Figure captions

5.2 (a) Single crystal of neodymium samarium hydrogen selenite x 50

5.2 (b) Single crystal of samarium hydrogen selenite x 50

5.2 (c) A needle crystal of praseodymium neodymium hydrogen selenite x 50

5.2 (d) A spherulite growth of praseodymium hydrogen selenite x 50

5.2 (e) Twinned crystal of praseodymium samarium hydrogen selenite x 50

5.2 (f) Striations observed on the surface of neodymium samarium hydrogen selenite crystal x 100

5.2 (g) Etch pattern produced by 10% $HNO_3$ for 30 sec on 100 plane of samarium hydrogen selenite crystal x 100

5.2 (h) Growth of samarium hydrogen selenite crystals in silica gel

5.2 (i) The samarium hydrogen selenite crystals

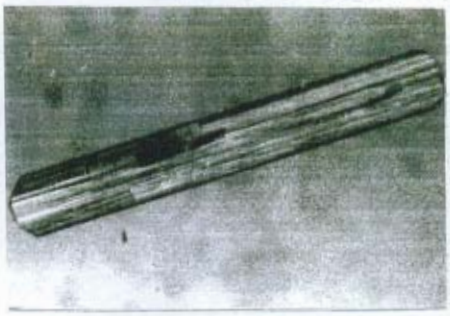

Fig. 5.2 (a)

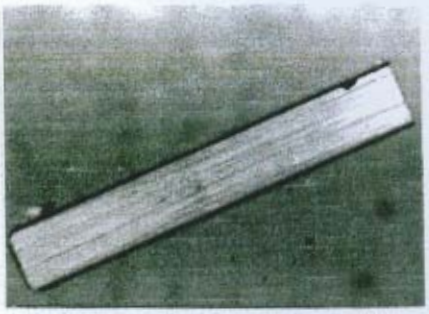

Fig. 5.2 (b)

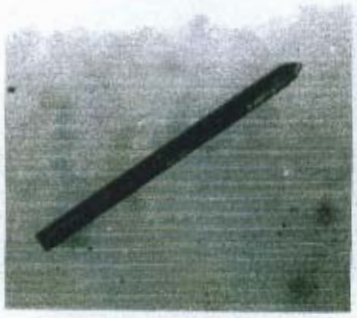

Fig. 5.2 (c)

Fig. 5.2 (d)

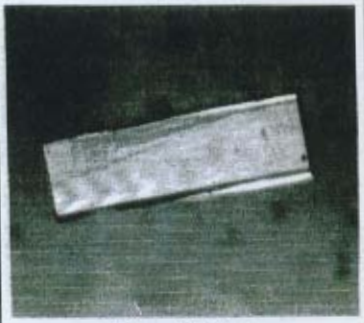

Fig. 5.2 (e)

Fig. 5.2 (f)

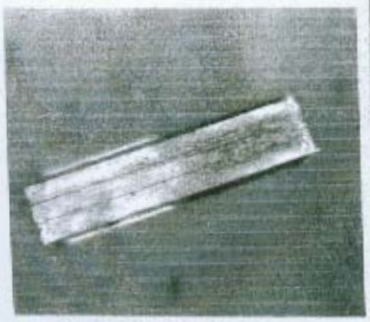

Fig. 5.2 (g)

Fig. 5.2 (h)

Fig.5.2 (i)

Fig. 5.2. Different morphologies and etch pattern of grown crystals.

Since these crystals are fragile, extreme care has to be taken in handling them. More details on these crystals are given in chapter 4. The crystals are observed to become semitransparent when they grow big in size. This may be due to the incorporation of defects in the initial stage of growth, which will progressively multiply during the growth.

The microphotographs of the crystal surface delineate of the surface features of the crystal and provide lot of information on the last stages of growth. Growth at different stages can be observed by etching studies of the crystal. It also reveals the defects formed during growth.

In particular, etching technique is a powerful tool for studying the nature of crystal dislocation. Gilmann and Keith[2] and Gilmann and Jhontson[3] showed that the etch pits nucleate at the points of emergence of dislocations and the other defects on the crystal surfaces. Moreover this technique is found to be very useful for studying the identification, origin and characterisation of defects such as grain boundaries, slip-lines, dislocations, stacking faults, volume indentation vacancies etc. Etching of the crystal surface yields etch figures and dissolution layers on its surfaces without losing its micro-morphology.

Etching study have been made on these crystals by selecting dilute nitric acid (10%) as etchant. These studies show etch pits arranged in parallel lines parallel to the longer edges of the crystal (fig. 5.2). Higher magnification showed that these pits are rectangular in shape, deep and with pointed bottom. These etch pits reveal the defects segregated along the major axis of the crystal.

## 5.3 Spectroscopic analysis

### 5.3.1 X-ray analysis

X-ray diffraction is one of the tools to determine the structure of the crystal. In this particular case the powder diffraction method has been employed for the study. Moreover single crystal analysis has been utilised to determine the structure parameters of the crystal. All the crystals are found to be monoclinic.

It is quite interesting to note that very little work has been reported in the literature on the structure of these crystals. Structure reports of mixed crystals do not exist at all. Powder patterns of PHS, NHS and SHS crystals given in fig.5.3 and the unit cell data of the above crystals were given in table 5.1-5.4. The X-ray powder diffraction pattern of mixed crystal is shown in fig.5.4 and diffraction data in table 5.5-5.7 It may be noted that 'd' values depend on the atomic dimension of the constituent atoms.

Single crystal data of PNHS, PSHS and NSHS have been collected and the data analysed. It is found that these groups of crystals are monoclinic with space group $P2_1/C$. The cell dimensions of these crystals vary slightly. This may be ascribed to the effect of lanthanide contraction. The volume of the unit cell decreases from PNHS to NSHS as expected.

**Table. 5.1 The cell parameters of the praseodymium, neodymium, samarium hydrogen crystals**

| Crystal | a ($\mathring{A}$) | b ($\mathring{A}$) | c ($\mathring{A}$) | β (deg) | Volume ($\mathring{A}^3$) |
|---|---|---|---|---|---|
| Pr | 11.254 | 9.632 | 10.333 | 114.31 | 1020.56 |
| Nd | 11.191 | 9.612 | 10.257 | 114.23 | 1005.97 |
| Sm | 11.108 | 9.621 | 10.155 | 114.19 | 989.97 |

**Table. 5.2 XRD data of praseodymium hydrogen selenite crystals**

| 2θ | d(nm) | Intensity (I) | $I/I_0$ |
|---|---|---|---|
| 21.474 | 4.138 | 301 | 58.22 |
| 25.258 | 3.526 | 108 | 20.8897 |
| 29.379 | 3.040 | 41 | 7.93303 |
| 32.520 | 2.753 | 517 | 100.00 |
| 35.196 | 2.550 | 75 | 14.5067 |
| 40.284 | 2.239 | 23 | 4.4487 |
| 43.899 | 2.062 | 21 | 4.0618 |
| 45.961 | 1.975 | 38 | 7.3500 |
| 48.563 | 1.875 | 25 | 4.8355 |
| 51.647 | 1.770 | 28 | 5.4158 |
| 54.285 | 1.690 | 45 | 8.7041 |
| 55.758 | 1.649 | 66 | 12.7659 |
| 57.538 | 1.602 | 61 | 11.7988 |

**Table. 5.3 XRD data of neodymium hydrogen selenite crystals**

| 2θ | d(nm) | Intensity (I) | $I/I_0$ |
|---|---|---|---|
| 17.801 | 4.983 | 15 | 19.2307 |
| 21.411 | 4.150 | 43 | 55.1282 |
| 23.430 | 3.797 | 17 | 21.7948 |
| 25.233 | 3.528 | 65 | 83.3333 |
| 27.074 | 3.294 | 18 | 23.0769 |
| 29.177 | 3.061 | 48 | 61.5384 |
| 30.994 | 2.885 | 19 | 24.3589 |
| 32.488 | 2.756 | 78 | 100.00 |
| 34.931 | 2.569 | 24 | 30.7692 |
| 46.024 | 1.972 | 19 | 24.3589 |
| 48.307 | 1.884 | 19 | 24.389 |
| 57.330 | 1.607 | 16 | 20.5128 |

**Table. 5.4 XRD data of samarium hydrogen selenite crystals**

| 2θ | d(nm) | Intensity (I) | $I/I_0$ |
|---|---|---|---|
| 21.583 | 4.117 | 895 | 73.7840 |
| 25.398 | 3.507 | 70 | 5.7708 |
| 30.088 | 2.970 | 56 | 4.6166 |
| 32.670 | 2.741 | 1213 | 100.00 |
| 35.350 | 2.539 | 36 | 2.9678 |
| 46.100 | 1.969 | 48 | 3.9571 |
| 48.541 | 1.876 | 37 | 3.0502 |
| 55.962 | 1.643 | 79 | 6.5127 |
| 57.774 | 1.596 | 39 | 3.215 |

**Table. 5.5 XRD data of praseodymium neodymium hydrogen selenite crystals**

Sp.gr. $-P2_1/c$ a=11.2189 $\mathring{A}$ b= 9.6349 $\mathring{A}$ c=10.2916 $\mathring{A}$ β=114.399 V=1013.1 $\mathring{A}^3$

| 2θ | d(nm) | Intensity (I) | $I/I_0$ |
|---|---|---|---|
| 21.067 | 4.217 | 74 | 80.4347 |
| 24.871 | 3.580 | 56 | 60.8695 |
| 26.690 | 3.339 | 26 | 28.2608 |
| 29.180 | 3.061 | 41 | 44.5652 |
| 32.127 | 2.786 | 92 | 100.00 |
| 34.778 | 2.580 | 25 | 27.1739 |

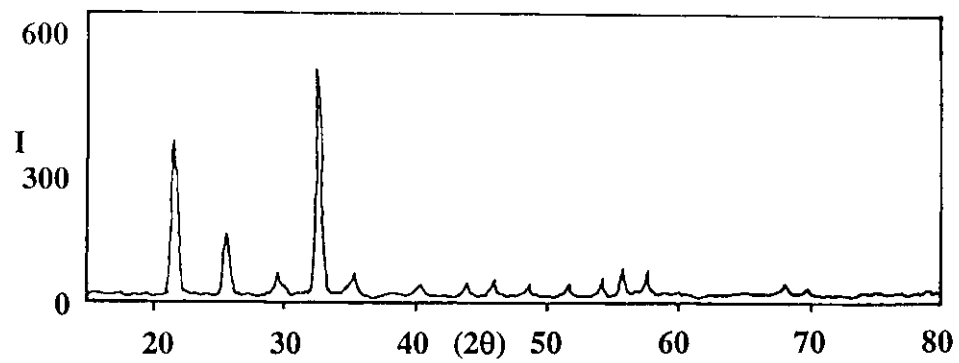


Fig.5.3(a) The X-ray powder pattern of PHS

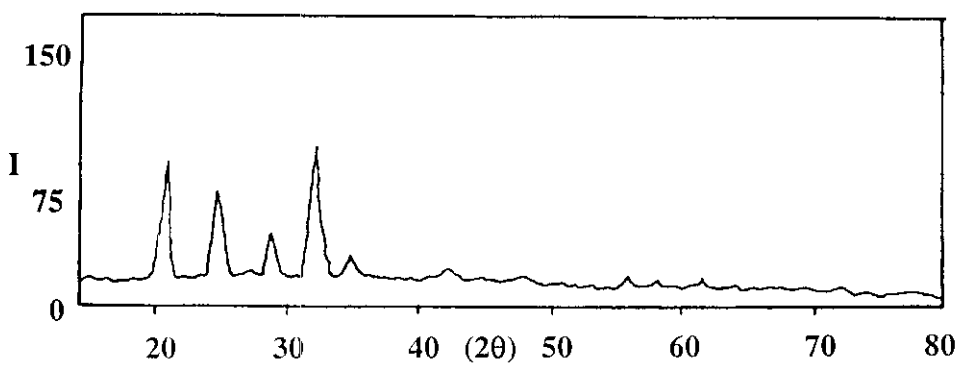


Fig.5.3 (b) The X-ray powder pattern of NHS

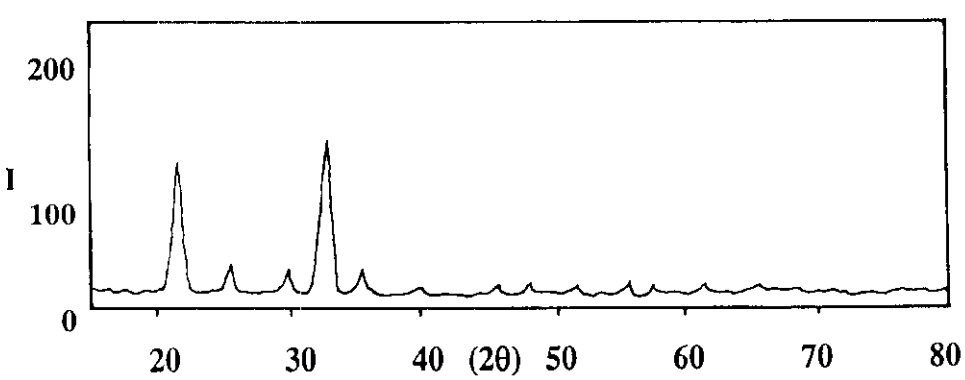


Fig.5.3 (c) The X-ray powder pattern of SHS

**Table. 5.6 XRD data of praseodymium samarium hydrogen selenite crystals**

Sp.gr. =$P2_1/c$ a=11.2422 $\mathring{A}$ b= 9.6127 $\mathring{A}$ c=10.2501 $\mathring{A}$ β=114.849 V=1005.2 $\mathring{A}^3$

| 2θ | d(nm) | Intensity (I) | $I/I_0$ |
|---|---|---|---|
| 21.662 | 4.103 | 965 | 100.00 |
| 25.476 | 3.496 | 96 | 9.94 |
| 29.635 | 3.015 | 40 | 4.145 |
| 32.722 | 2.737 | 698 | 72.3316 |
| 35.399 | 2.536 | 46 | 4.7668 |
| 55.959 | 1.643 | 39 | 4.0414 |
| 57.77 | 1.596 | 42 | 4.3523 |

**Table. 5.7 XRD data of neodymium samarium hydrogen selenite crystals**

Sp.gr.=$P2_1/c$ a=11.1457 $\mathring{A}$ b= 9.6337 $\mathring{A}$ c=10.2022 $\mathring{A}$ β=114.444 V=997.3 $\mathring{A}^3$

| 2θ | d(nm) | Intensity (I) | $I/I_0$ |
|---|---|---|---|
| 21.9 | 4.122 | 610 | 100 |
| 25.2 | 3.513 | 51 | 8.3 |
| 30 | 3.828 | 520 | 5.24 |
| 32.5 | 2.742 | 62 | 10.16 |
| 34.98 | 2.540 | 51 | 8.3 |
| 37.5 | 2.399 | 50 | 8.1 |
| 41 | 2.212 | 50 | 8.1 |
| 46.8 | 1.984 | 51 | 8.3 |
| 48 | 1.976 | 51 | 8.3 |
| 57 | 1.844 | 52 | 8.5 |

### 5.3.2 Infrared spectra of crystals

Infrared radiation promotes transitions in a molecule between rotational and vibrational energy levels of the ground electronic energy states. It is an important study in the investigation of the molecular structure of the crystals. The thermogravimetric and X-ray studies complement the FT-IR studies to find exact structure and molecular formula of the crystals. Information on physico-chemical properties of the trivalent rare earth and hydrogen selenite ions are scanty in literature. It is observed in the present investigation that all the grown crystals show almost identical vibrational modes and some have slight shift, which can be attributed to the presence of constituent rare earth elements.

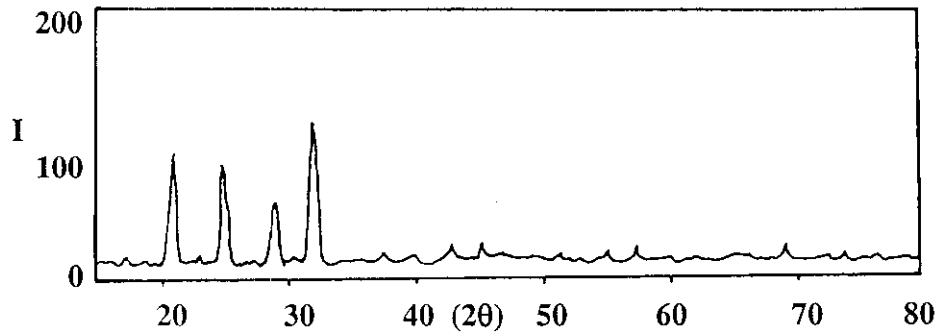


Fig. 5.4 (a) The X-ray powder pattern of PNHS

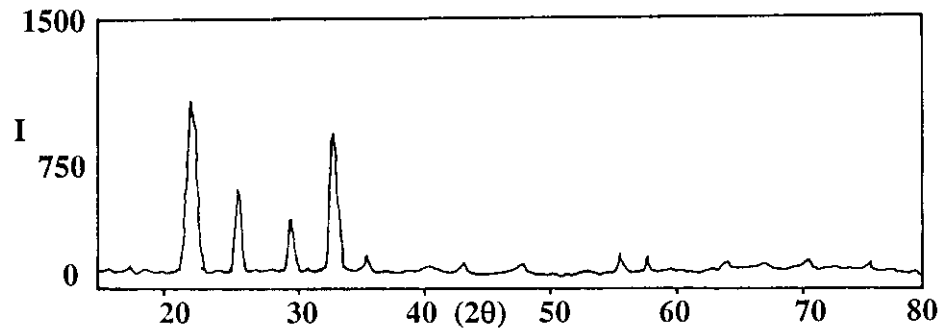


Fig. 5.4 (b) The X-ray powder pattern of PSHS

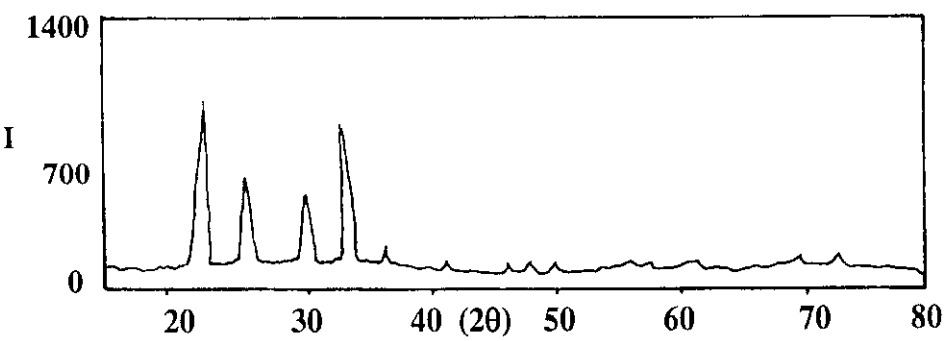


Fig. 5.4 (c) The X-ray powder pattern of NSHS

The FT-IR spectra of the crystalline samples were recorded by the KBr pellet method. The powdered crystal samples are mixed with KBr (IR- grade) in the ratio of about 0.6 mg of the sample per 300 mg of KBr, pressed into a pellet under a pressure of 8 ton and spectra is recorded by the use of Shimadzu FTIR-8101A spectrophotometer. For identifying the $HSeO_3$, $SeO_3$ and HOH, groups, the range of wave numbers used was between 400 and 4000 $cm^{-1}$.

The absorption bands in the spectrum of praseodymium hydrogen selenite, neodymium hydrogen selenite and samarium hydrogen selenite show small differences in the band regions which shows that the rare earth element is contributing to a very small shift in the finger print band region of those particular group frequencies. The bands at 3500-3100$cm^{-1}$ are due to the vibration of the water molecule. The $SeO_3^{2-}$ vibrations lie in between 840$cm^{-1}$and 440$cm^{-1}$. A very significant band at 1227$cm^{-1}$ is ascribed to hydrogen selenite ($HSeO_3^-$). The bands at 1640$cm^{-1}$ and 2405$cm^{-1}$ show the presence of OH molecules. The FT-IR spectra recorded for mono rare earth hydrogen selenite crystals are shown in the fig 5.5 The corresponding assignments for the functional groups are given in the table. 5.8.

The FT-IR absorption spectra of the mixed rare earth hydrogen selenites are shown in fig. 5.6. It is worth noting that, there is a frequency shift in the spectrum. It may be due to the bonding of the rare earth atom to the selenium and oxygen atoms.

X-ray analysis shows that all the grown crystals are monoclinic with space group $P2_1/c$. In all the rare earth hydrogen selenite crystals there exist six co-ordinated rare earth atoms and two different selenite groups, which are hydrogen selenite and pure selenite . Both hydrogen selenite and selenite act as a bidentate and bridging ligands[4]

.

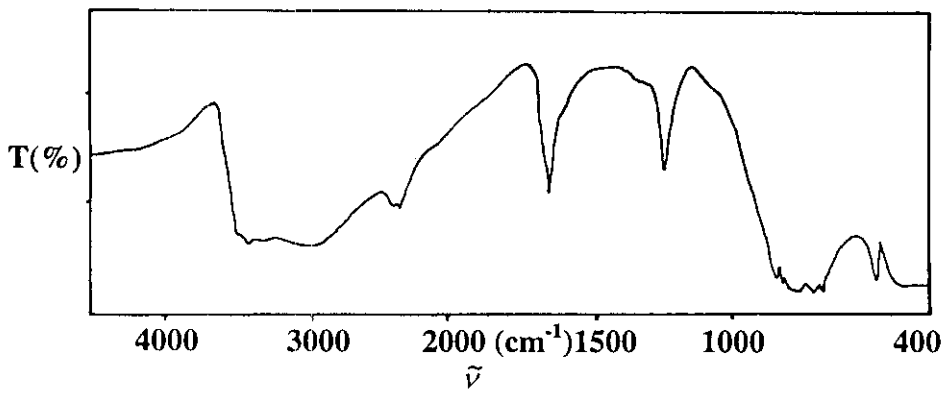


Fig. 5.5 (a) The FT-IR spectra of PHS

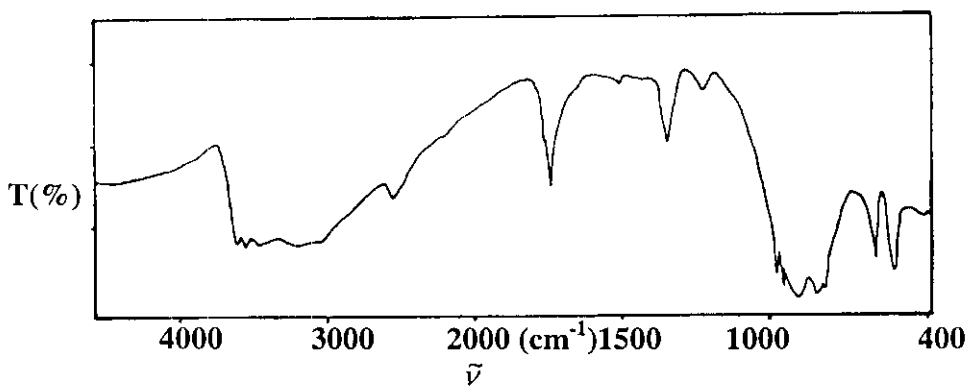


Fig. 5.5 (b) The FT-IR spectra of NHS

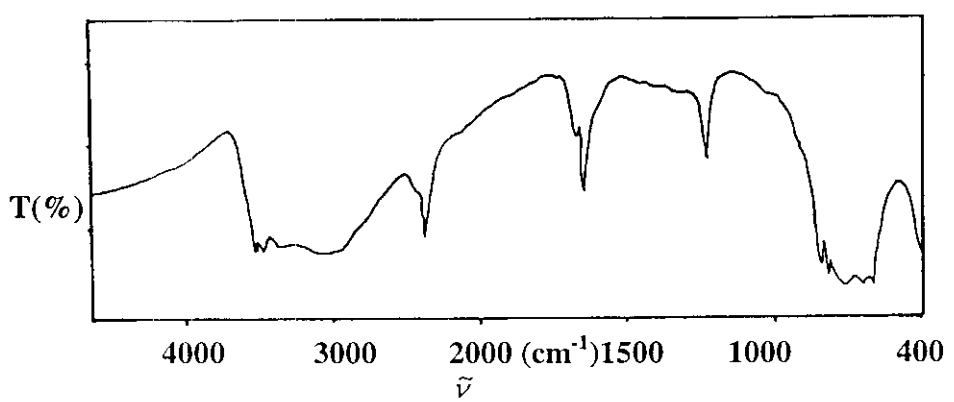


Fig. 5.5 (c) The FT-IR spectra of SHS

**Table. 5.8 Spectral data and band assignments of rare earth hydrogen selenite crystals**

| IR ( $\tilde{\nu}$ ) $cm^{-1}$ | Assignments |
|---|---|
| 437 -s | $\nu_2(SeO_3^{2-})$ |
| 493 -s | $\nu$(Se-O) |
| 670 -s | $\delta$(Se-OH) |
| 700 -s | $\nu_1(HSeO_3^{2-})$ |
| 755 -s | $\nu_3$(Se-O) |
| 820 -m | $\nu_1(SeO_3^{2-})$ |
| 843 -m | $\nu_1(HSeO_3^{-})$ |
| 1227 -s | $\delta$(O-Se-OH) |
| 1640 -s | $\delta$(O-Se-OH) |
| 2406 -s | $\nu$(OH) |
| 3447 -w | $\nu$(OH) |

s-strong m-medium w-weak

### 5.3.3 UV-Visible absorption and emission spectra of rare earth hydrogen selenites

In the periodic table the rare earth elements are broadly classified into two groups, each of fourteen elements, known as lanthanides and actinides. The electronic configuration of these elements, which characterise them, is the progressive filling of the 4f or 5f shells for the lanthanides and actinides, respectively. Lanthanides which are associated with the filling of 4f shell begin with cerium (Ce, Z = 58) and end with Lutetium (Lu, Z=71) whereas actinides which are associated with the filling of 5f shell, begin with thorium (Th, Z=90) and ends with the element Lawrencium (Lw, Z =103). Commonly the natural lanthanides shows the feature of an inert gas xenon structured electronic configuration ($1s^2\ 2s^2\ 2p^6\ 3s^2\ 3d^{10}\ 4s^2\ 4d^{10}\ 5s^2\ 5p^6$ ) with two or three outer electrons ($6s^2$ or 5d $6s^2$).

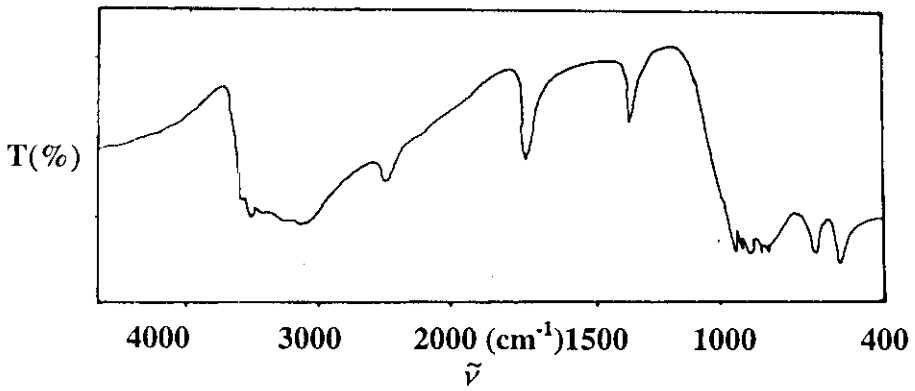


Fig. 5.6 (a) The FT-IR spectra of PNHS

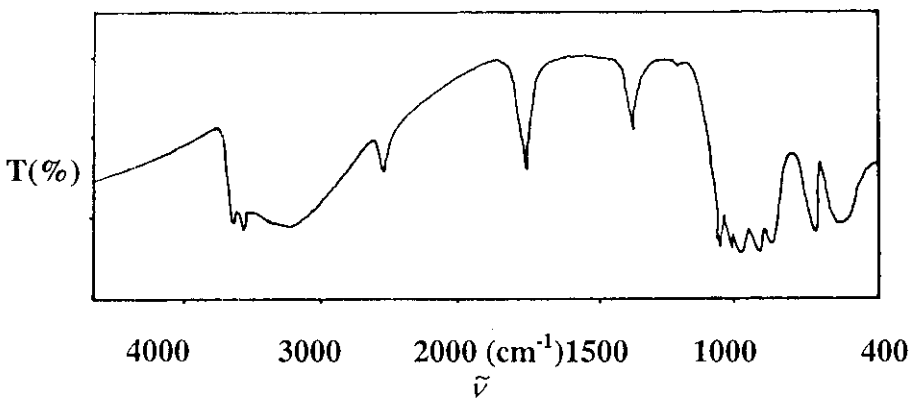


Fig. 5.6 (b) The FT-IR spectra of PSHS

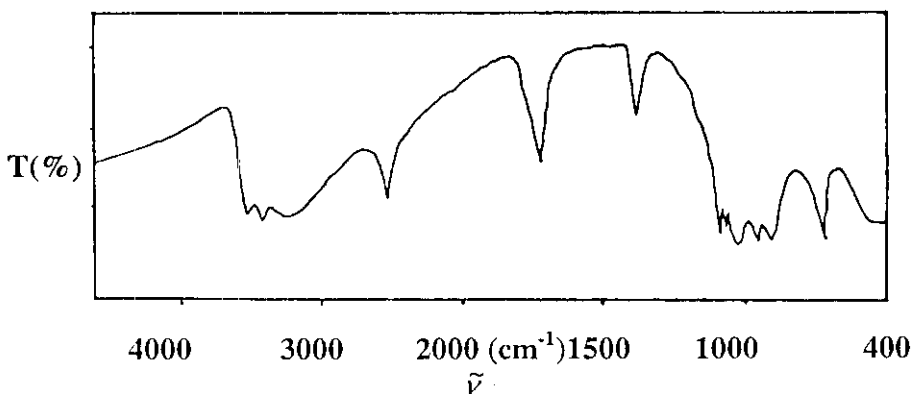


Fig. 5.6 (c) The FT-IR spectra of NSHS

It is found that the commencement of the lanthanide series is characterised by a deep potential near the nucleus for the 4f electrons and hence they are drawn from the outer shells of the atom into the interior. This happens as a result of the imperfect shielding of one 4f shell by another 4f electron[5] and the phenomenon is called lanthanide contraction. As we proceed through the lanthanide series, the nuclear charge together with the number of 4f electrons increases one at each step because of the shielding of 4f electrons with each increase, the effective nuclear charge increases then causing a reduction of entire $4f^N$ shells.

**Table. 5.9 Spectroscopic data of trivalent rare earth ions used for growth**

| Element | Atomic number | Spin | μ | Ground state |
|---|---|---|---|---|
| Praseodymium | 59 | 5/2 | 3.9 | $3H_4$ |
| Neodymium | 60 | 7/2 | -1.03 | $4I_{9/2}$ |
| Samarium | 62 | 7/2, 5/2 | - 0.83, - 0.69<br>1.6, 3.6 | $6H_{5/2}$ |

The lanthanides may be ionised by the successive removal of electrons. The first stage of ionisation, with the exception of lutetium results from the removal of a 6s electron. In the second stage of ionisation, the removal of a further 6s electron occurs and at the third stage, all the 6s and 5d electrons, and frequently a 4f electron, have been removed to leave, apart from the xenon structure, a $4f^N$ configuration where N = 1 for cerium increase regularly to N = 14 for lutetium[6,7,8,9].

The absorption spectra of the rare earths in the optical region arise from the transition within the $4f^N$ configuration. Due to the shielding habit of the $5s^2$ $5p^6$ shells, perturbation by surrounding neighbours does not take place resulting in a sharp line spectra[10]. However the observed spectra are found to be extremely complex in nature[11].

The absorption and emission spectra of the grown rare earth hydrogen selenite crystals are recorded. The UV-Visible NIR region absorption spectra of the samples are recorded on a Shimadzu 160A spectrophotometer. All the spectra of the samples

were taken in ambient temperature. The spectra are shown in the fig.5.7-5.8. The presence of rare earth ion and its transition levels are assigned in the tables 5.10-5.15

**Table. 5.10 Assignments of UV-Visible NIR absorption spectrum of praseodymium hydrogen selenite**

| Ion | Wavelength (nm) | Energy ($cm^{-1}$) | Assignments |
|---|---|---|---|
| $Pr^{3+}$ | 446 | 22242 | $^3P_2$ |
| | 472 | 21186 | $^3P_1$ |
| | 490 | 20408 | $^3P_0$ |
| | 597 | 16750 | $^1D_2$ |

**Table. 5.11 Assignments of UV-Visible NIR absorption spectrum of neodymium hydrogen selenite**

| Ion | Wavelength (nm) | Energy ($cm^{-1}$) | Assignments |
|---|---|---|---|
| $Nd^{3+}$ | 357 | 28011 | $^4D_{5/2}$ |
| | 470 | 21276 | $^4G_{11/2}$ |
| | 510 | 19607 | $^4G_{9/2}$ |
| | 530 | 18867 | $^4G_{7/2}$ |
| | 580 | 17241 | $^4G_{5/2}$ |
| | 680 | 14705 | $^4F_{9/2}$ |
| | 755 | 13245 | $^4S_{5/2}$ |
| | 800 | 12500 | $^2H_{9/2}$ |
| | 870 | 11494 | $^4F_{3/2}$ |

The absorption spectra of $Nd^{3+}$, $Pr^{3+}$ and $Sm^{3+}$ ions in the various mixed crystals are shown in fig.5.8. In the absorption spectra the transition due to $Nd^{3+}$, $Pr^{3+}$ and $Sm^{3+}$ are identified and are represented by the respective spectral terms for the $Nd^{3+}$, $Pr^{3+}$ and $Sm^{3+}$ . The transition occur from the ground levels; $^4I_{9/2}$, $^3H_4$ and $^6H_{5/2}$ for $Nd^{3+}$, $Pr^{3+}$ and $Sm^{3+}$ ions respectively. The assignments for all the crystals are also given in the tables.

**Table. 5.12 Assignments of UV-Visible NIR absorption spectrum of samarium hydrogen selenite**

| Ion | Wavelength (nm) | Energy ($cm^{-1}$) | Assignments |
|---|---|---|---|
| $Sm^{3+}$ | 375 | 26666 | $^4K_{11/2}$ |
| | 403 | 24813 | $^4L_{13/2}$ |
| | 472 | 20964 | $^4I_{11/2}$ |
| | 948 | 10548 | $^6F_{11/2}$ |
| | 1086 | 9208 | $^6F_{9/2}$ |

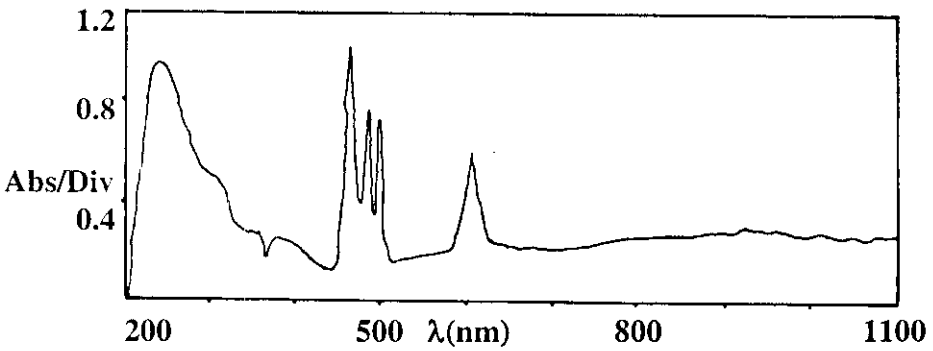


Fig. 5.7 (a) The UV-Visible absorption spectrum of PHS

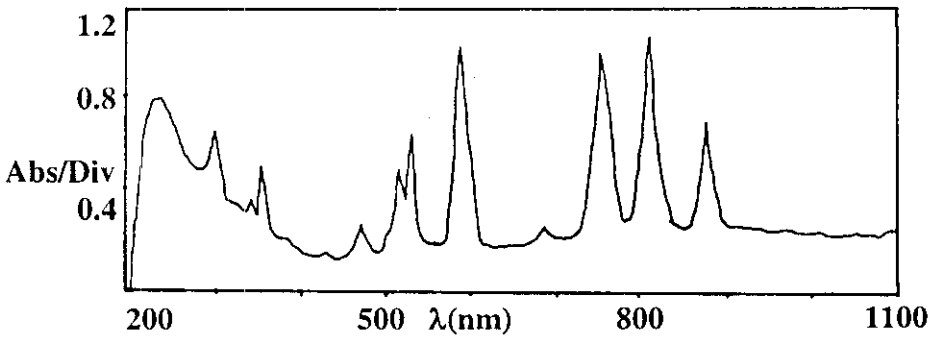


Fig. 5.7 (b) The UV-Visible absorption spectrum of NHS

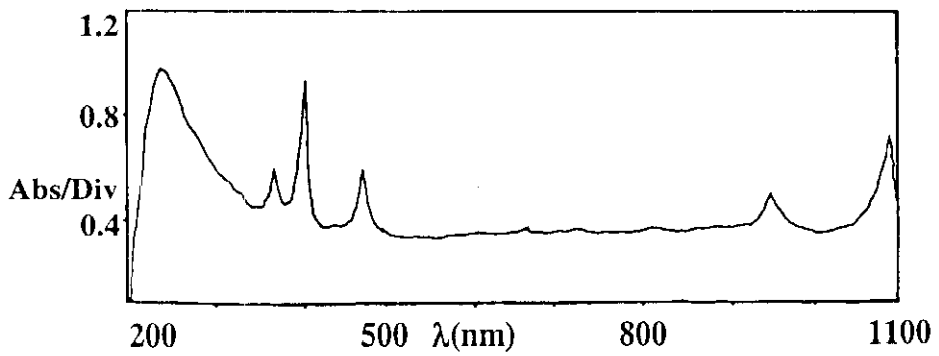


Fig. 5.7 (c) The UV-Visible absorption spectrum of SHS

**Table. 5.13 Assignments of UV-Visible NIR absorption spectrum of praseodymium neodymium hydrogen selenite**

| Ion | Wavelength (nm) | Energy ($cm^{-1}$) | Assignments |
|---|---|---|---|
| $Pr^{3+}$ | 447 | 22371 | $^3P_2$ |
| | 472 | 21186 | $^3P_1$ |
| | 597 | 16750 | $^1D_2$ |
| $Nd^{3+}$ | 580 | 17241 | $^4G_{5/2}$ |
| | 751 | 13315 | $^4S_{3/2}$ |
| | 803 | 12453 | $^2H_{9/2}$ |
| | 870 | 11494 | $^4I_{3/2}$ |

**Table. 5. 14 Assignments of UV-Visible NIR absorption spectrum of praseodymium samarium hydrogen selenite**

| Ion | Wavelength (nm) | Energy ($cm^{-1}$) | Assignments |
|---|---|---|---|
| $Pr^{3+}$ | 472 | 21186 | $^3P_1$ |
| | 596 | 16778 | $^1D_2$ |
| | 1043 | 9587 | $^1G_4$ |
| $Sm^{3+}$ | 402 | 24875 | $^4F_{9/2}$ |
| | 445 | 22471 | $^4G_{7/2}$ |
| | 948 | 10548 | $^6F_{11/2}$ |
| | 1086 | 9208 | $^6F_{9/2}$ |

**Table. 5.15 Assignments of UV-Visible NIR absorption spectrum of neodymium samarium hydrogen selenite**

| Ion | Wavelength (nm) | Energy ($cm^{-1}$) | Assignments |
|---|---|---|---|
| $Nd^{3+}$ | 526 | 19011 | $^4G_{7/2}$ |
| | 580 | 17241 | $^4G_{5/2}$ |
| | 751 | 13315 | $^4S_{3/2}$ |
| | 803 | 12453 | $^2H_{9/2}$ |
| | 870 | 11494 | $^4I_{3/2}$ |
| $Sm^{3+}$ | 403 | 24813 | $^4L_{13/2}$ |
| | 480 | 20833 | $^4I_{11/2}$ |
| | 1086 | 9208 | $^6F_{9/2}$ |

An experimental set up as shown in fig. 5.9 has been designed to record the emission spectra of the samples. Here the excitation source is a fibre coupled nitrogen laser, which can deliver pulses of 7ns duration, having an average power 25mw and frequency 100Hz. The laser beam delivery system consists of a quartz lens of focal length 50mm and a silica fibre having a core diameter of 400 μm, 1.5 m in length.

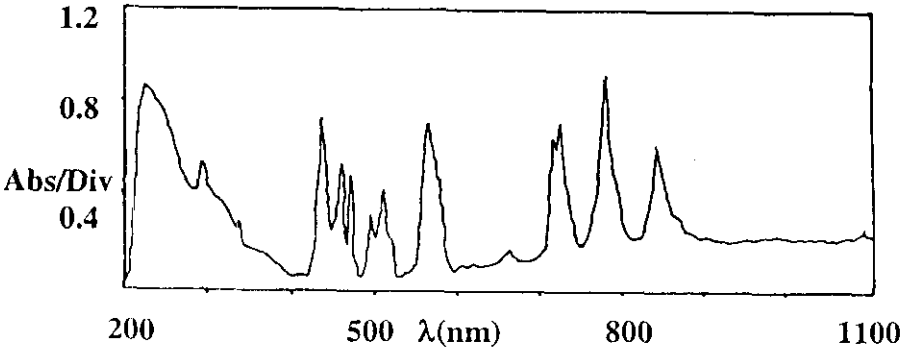


Fig. 5.8 (a) The UV-Visible absorption spectrum of PNHS

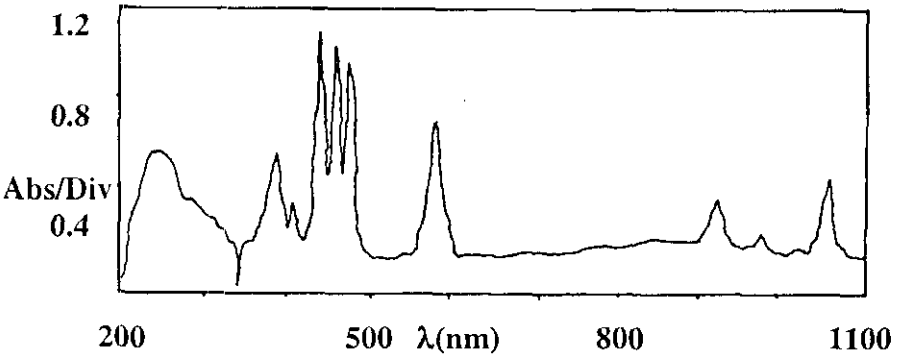


Fig. 5.8 (b) The UV-Visible absorption spectrum of PSHS

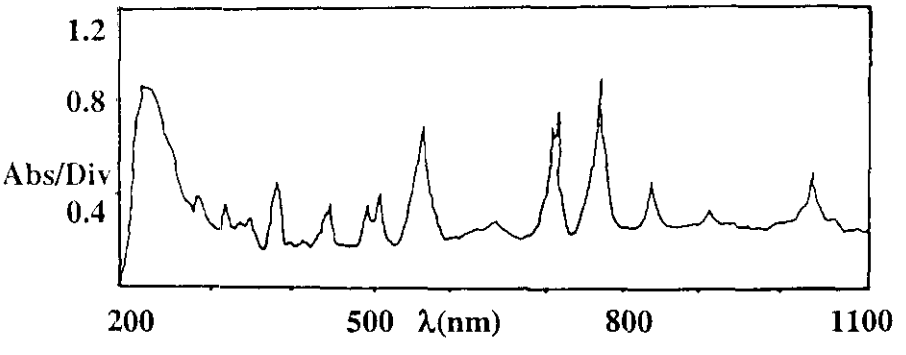


Fig. 5.8 (c) The UV-Visible absorption spectrum of PHS

A quartz lens focuses the nitrogen laser beam and the focussed beam is coupled to a silica core fibre mounted in the x-y-z moment. The laser beam emerging out of the fibre has average power about 1 mw. This is then allowed to fall on the sample and fluorescence emission is detected in a perpendicular direction using an efficient detection system consisting of a photodiode, pre-amplifier and photomultiplier tube and finally the signals are processed by a computer to obtain the emission spectra.

The emission spectra of the grown crystals are shown in fig.5.10-5.11 and their assignments are given in tables 5.16-5.21.

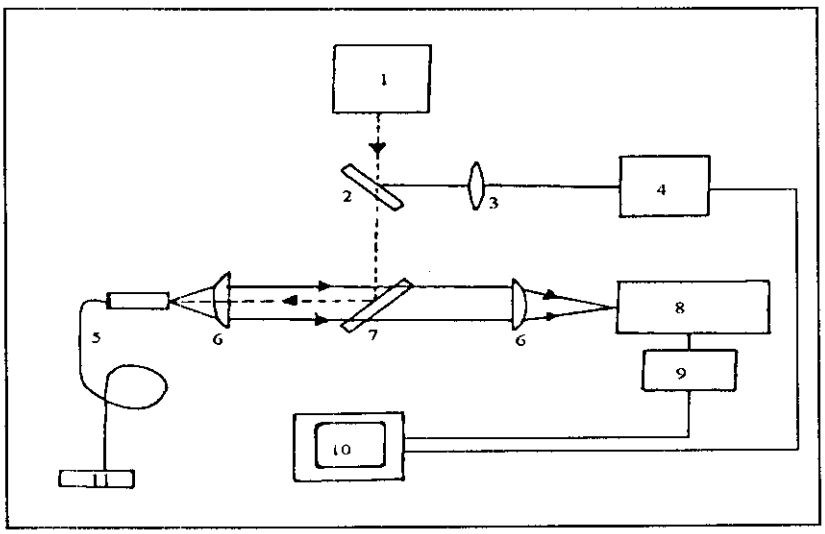


Fig. 5.9 The experimental set-up for emission spectral studies

1. $N_2$- laser 2&7. Beam splitters. 3. Focussing lens. 4. Photo diode. 5. Optical filter. 6. Cylindrical lens. 8. Monochromator. 9. Photomultiplier tube. 10. Microcomputer. 11. Sample.

**Table. 5.16 Assignments of emission spectra of praseodymium hydrogen selenite**

| Ion | Wavelength (nm) | Energy ($cm^{-1}$) | Assignments |
|---|---|---|---|
| $Pr^{3+}$ | 444 | 22535 | $3P_2$ |
| | 465 | 21500 | $1I_6$ |
| | 469 | 21330 | $3P_1$ |
| | 489 | 20750 | $3P_0$ |

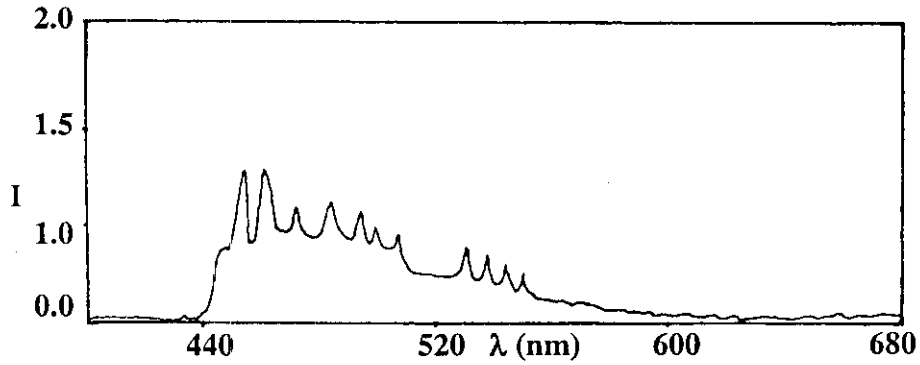


Fig. 5.10 (a) The emission spectrum of PHS

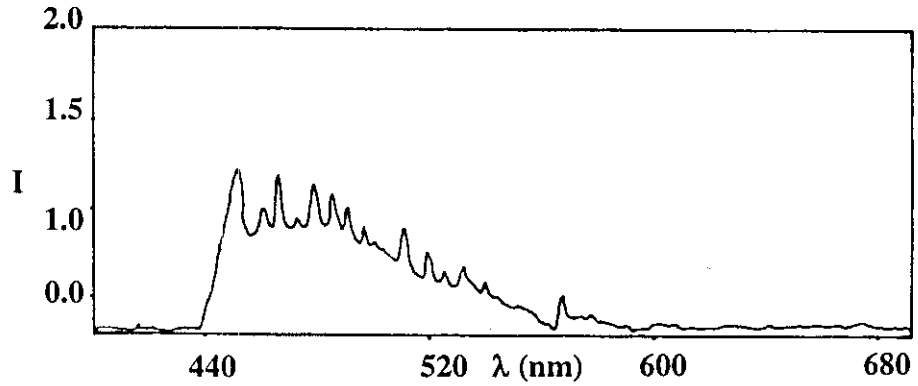


Fig. 5.10 (b) The emission spectrum of NHS

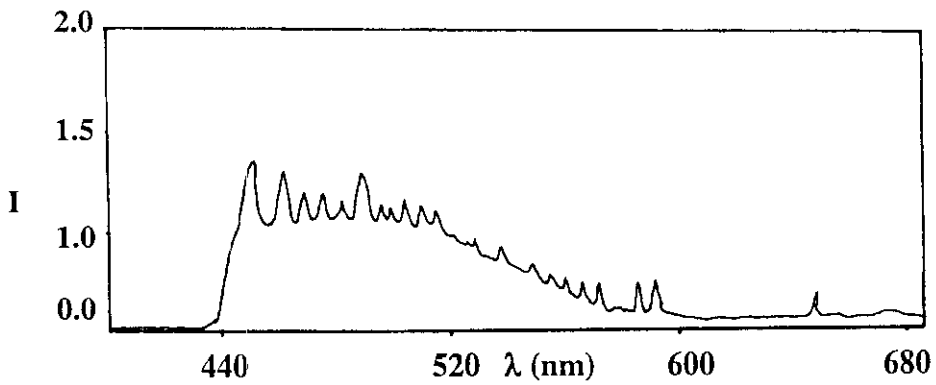


Fig. 5.10 (c) The emission spectrum of SHS

**Table. 5.17 Assignments of emission spectra of neodymium hydrogen selenite**

| Ion | Wavelength (nm) | Energy ($cm^{-1}$) | Assignments |
|---|---|---|---|
| $Nd^{3+}$ | 466 | 21426 | $^4G_{11/2}$ |
| | 474 | 21056 | $^2G_{9/2}$ |
| | 514 | 19434 | $^4G_{9/2}$ |
| | 528 | 19020 | $^4G_{7/2}$ |
| | 583 | 17135 | $^4G_{5/2}$ |

**Table. 5.18 Assignments of emission spectra of samarium hydrogen selenite**

| Ion | Wavelength (nm) | Energy ($cm^{-1}$) | Assignments |
|---|---|---|---|
| $Sm^{3+}$ | 452.53 | 22098 | $^4F_{5/2}$ |
| | 463.78 | 21562 | $^1I_{11/2}$ |
| | 485.44 | 20600 | $^1I_{9/2}$ |
| | 499.75 | 20010 | $^4G_{7/2}$ |
| | 529.38 | 18860 | $^4F_{7/2}$ |
| | 559.91 | 17860 | $^4G_{5/2}$ |

**Table. 5.19 Assignments of emission spectra of praseodymium neodymium hydrogen selenite**

| Ion | Wavelength (nm) | Energy ($cm^{-1}$) | Assignments |
|---|---|---|---|
| $Pr^{3+}$ | 465.35 | 21489 | $^1I_6$ |
| | 468.85 | 21329 | $^3P$ |
| $Nd^{3+}$ | 474.9 | 21426 | $^4G_{11/2}$ |
| | 474.92 | 21056 | $^2G_{9/2}$ |
| | 514.56 | 19434 | $^4G_{9/2}$ |

**Table. 5.20 Assignments of emission spectra of praseodymium samarium hydrogen selenite**

| Ion | Wavelength (nm) | Energy ($cm^{-1}$) | Assignments |
|---|---|---|---|
| $Pr^{3+}$ | 466.22 | 21449 | $^1I_6$ |
| | 481.86 | 20733 | $^3P_0$ |
| | 593.82 | 16840 | $^1D_2$ |
| $Sm^{3+}$ | 452.53 | 22098 | $^4F_{5/2}$ |
| | 485.39 | 20602 | $^1I_{9/2}$ |
| | 499.7 | 20012 | $^4G_{7/2}$ |
| | 530.14 | 18863 | $^4G_{5/2}$ |

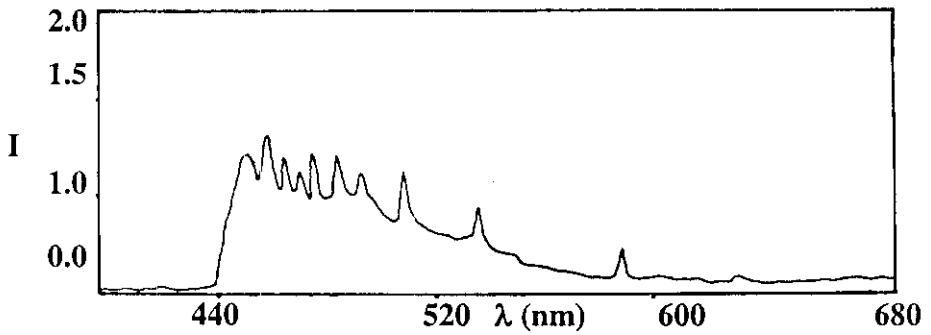


Fig. 5.11 (a) The emission spectrum of PNHS

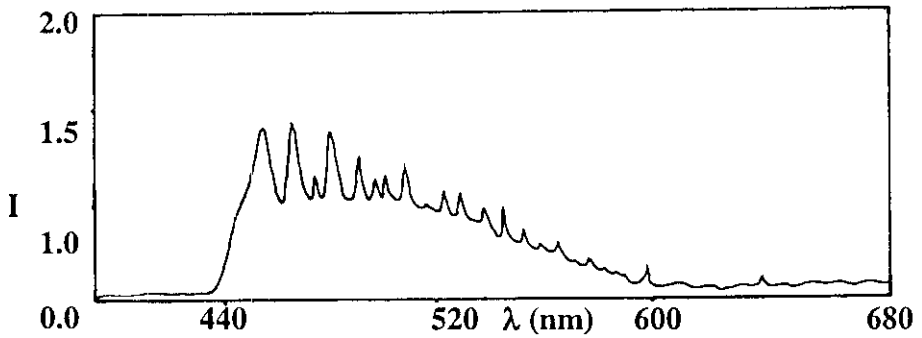


Fig. 5.11 (b) The emission spectrum of PSHS

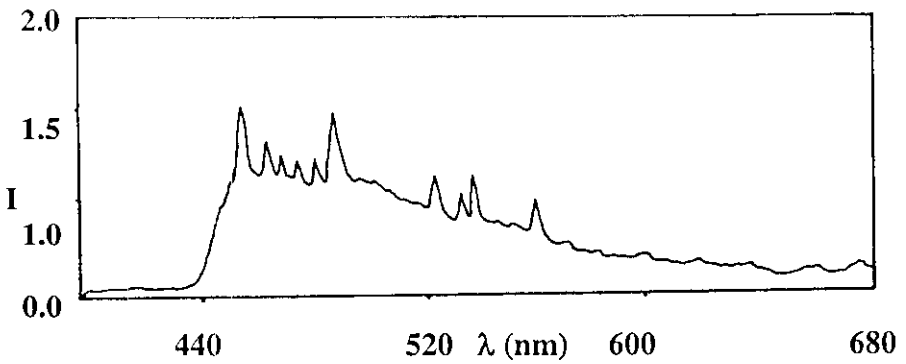


Fig. 5.11 (c) The emission spectrum of NSHS

**Table. 5.21 Assignments of emission spectra of neodymium samarium hydrogen selenite**

| Ion | Wavelength (nm) | Energy ($cm^{-1}$) | Assignments |
|---|---|---|---|
| $Nd^{3+}$ | 466.7 | 21427 | $^4G_{11/2}$ |
| | 474.9 | 21057 | $^2G_{9/2}$ |
| | 583.6 | 17135 | $^4G_{5/2}$ |
| $Sm^{3+}$ | 452.49 | 22100 | $^4F_{5/2}$ |
| | 463.78 | 21562 | $^1I_{11/2}$ |
| | 485.39 | 20602 | $^1I_{9/2}$ |
| | 530.27 | 18858 | $^4G_{5/2}$ |

## 5.4 Energy dispersive X-ray analysis (EDAX)

The structures and proposed chemical formulae of the crystals have been verified by using different analytical techniques. The proportion of the different rare earths present in the crystals are investigated by using which confirm the presence as well as the composition of the rare earth ions in the crystals.

In the energy dispersive X-ray analysis the sample is irradiated with high energy electrons. The energy of the consequent radiation emitted from the specimen is related to the atomic number of the elements present in the sample. The EDAX spectrum is a relation between intensity and binding energy of the emitted photoelectron. It is interesting to note that the peak height and area of the peaks are measures of the quantity of the elements incorporated in the specimen. Though this method is not very accurate, the comparison of the EDAX peaks of the two elements in the mixed rare earth hydrogen selenite; PNHS, PSHS and NSHS. The EDAX analysis for different stoichiometric combination of the crystals show that the properties of rare earth ions going into the crystals are almost in the ratio of supernatant reactants.

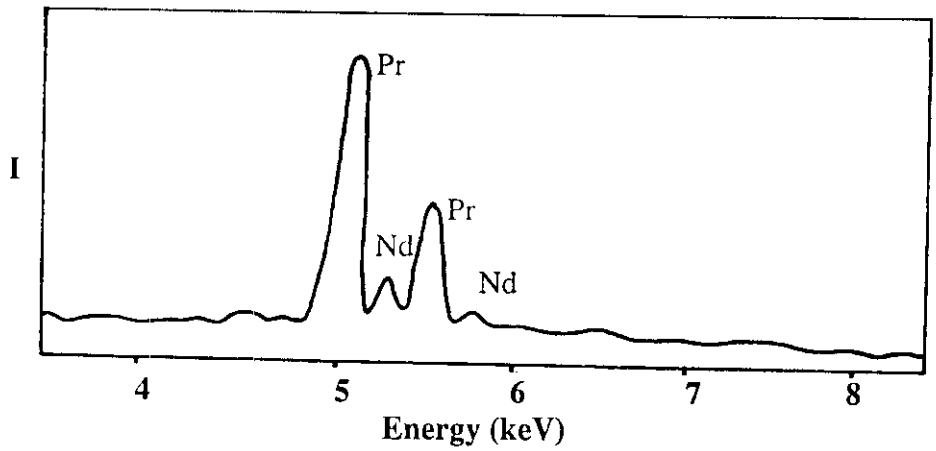


Fig. 5.12 (a) The EDAX pattern of PNHS (75:25) crystal

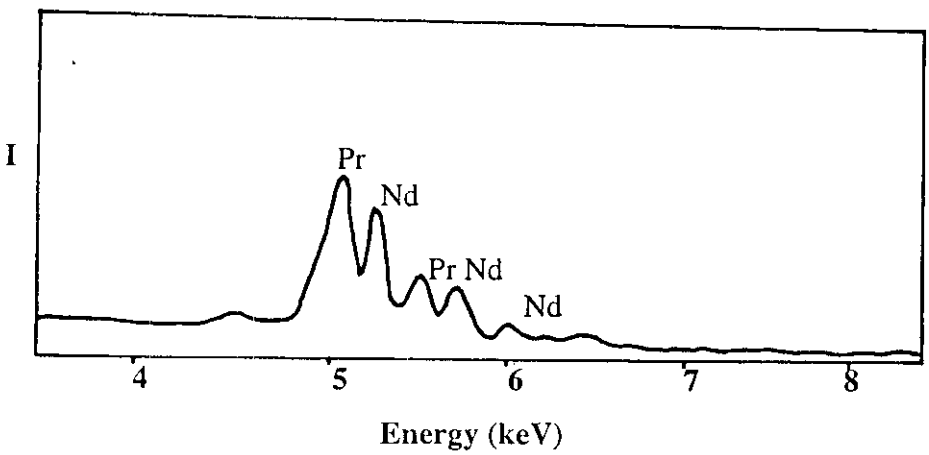


Fig. 5.12 (b) The EDAX pattern of PNHS (50:50) crystal

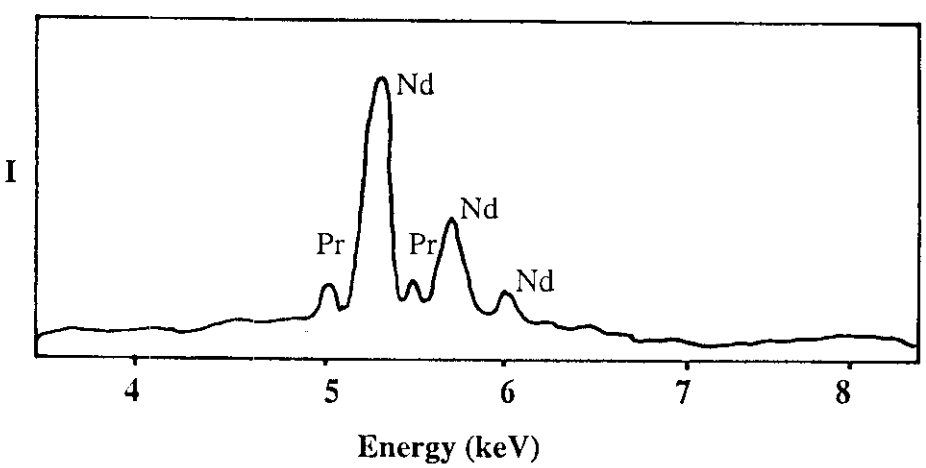


Fig. 5.12 (c) The EDAX pattern of PNHS (25:75) crystal

The EDAX analysis of the crystal samples have been carried out by using a Link AM 10,000 instrument and the quantitative analysis were carried out by employing ZAF 4/FLS program and using cobalt as the internal standard. The samples were prepared by powdering the crystals and palletising by using hydraulic press. The pellets of 1cm in diameter and 1mm in thick have been used for the studies.

### 5.4.1 EDAX of praseodymium neodymium hydrogen selenite

The praseodymium neodymium hydrogen selenite crystals (PNHS) grown by the diffusion of 0.5M solution of $Pr(NO_3)_3$ and $Nd(NO_3)_3$ by volume in the ratios 25:75, 50:50 and 75:25 have been selected for investigations. Fig.5.12 show the measured EDAX pattern. The presence of Pr and Nd is evident from the characteristic $L_\alpha$ and $L_\beta$ peaks for these elements. The presence of Nd in the specimen is evident from the peaks at 5.24, 5.74 and 6.03 keV which corresponds to $L_\alpha$, $L_{\beta 1}$ and $L_{\beta 2}$ peaks of Nd. The peaks at 5.08 and 5.49 keV correspond to $L_\alpha$ and $L_\beta$ lines of Pr. It is interesting to note that as the concentration of $Pr(NO_3)_3$ in the upper reactance change the heights (area) of the $L_\alpha$ and $L_\beta$ peaks of Pr goes on increasing. The similar variations are also observed for the peaks corresponding to Nd. The detailed results of the quantitative analysis of PNHS crystals with different stoichiometries are given in the table. 5.22

**Table. 5. 22 Summary of EDAX analysis of PNHS crystals**

| Expt. No. | Elements present in the mixed crystals | The ratio of the upper reactants (by volume) | The observed % of rare earths |
|---|---|---|---|
| 1 | Pr, Nd | 25 : 75 | 24.466, 76.534 |
| 2 | Pr, Nd | 50 : 50 | 48.144, 51.856 |
| 3 | Pr, Nd | 75 : 25 | 74.854, 25.146 |

The $L_\alpha$ and $L_\beta$ peaks of Pr and Nd observed in the EDAX pattern of PNHS crystal at their corresponding binding energy values confirms the presence of these elements. The values show that the incorporation of praseodymium and neodymium in the crystal is in the ratio of its presence in the supernatant solution follows the proportion of the rare earth ions present in the supernatant (upper reactant) solution.

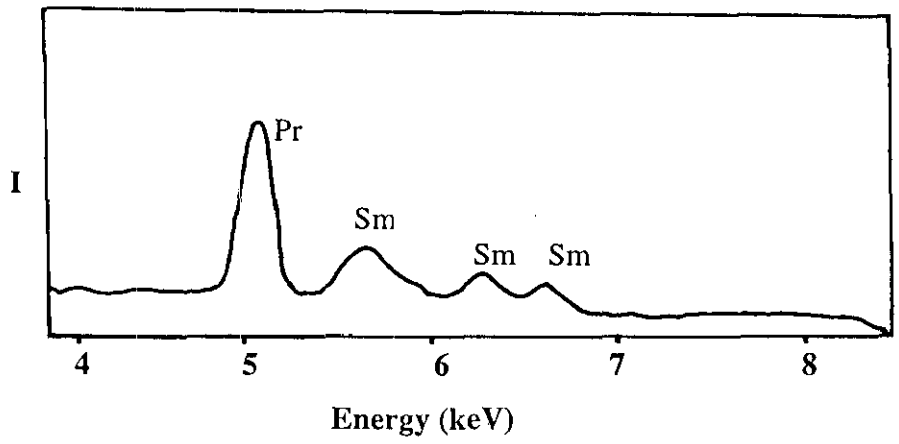


Fig. 5.13 (a) The EDAX pattern of PSHS (75:25) crystal

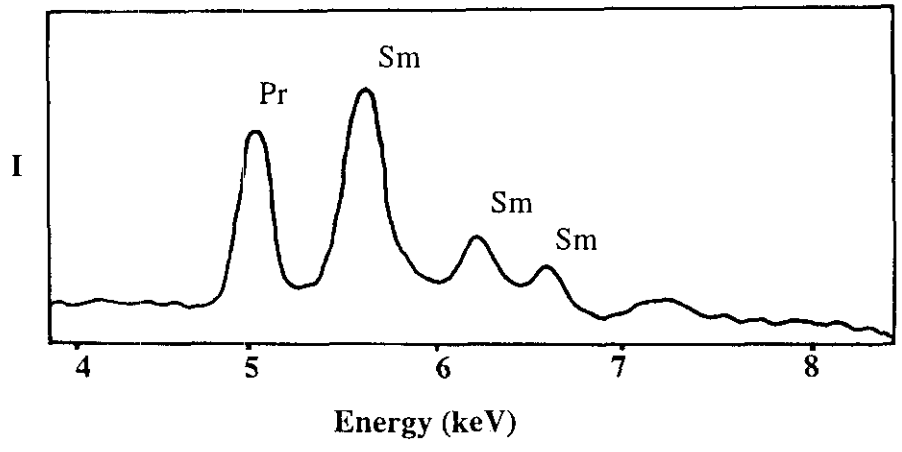


Fig. 5.13 (b) The EDAX pattern of PSHS (50:50) crystal

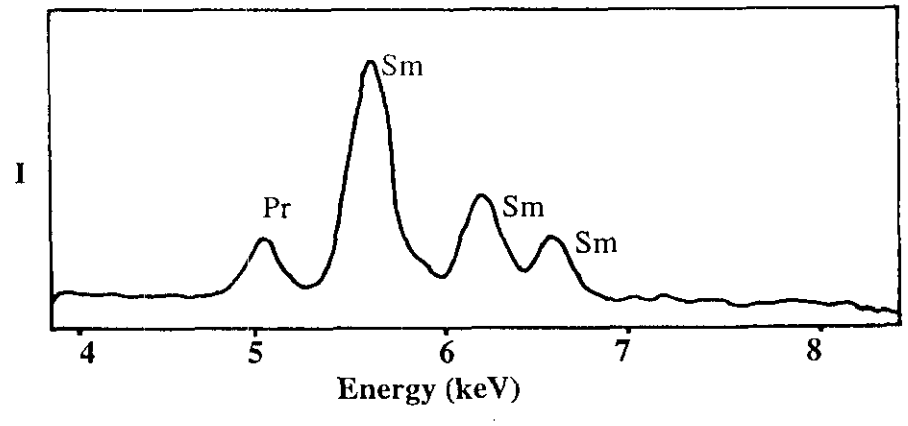


Fig. 5.13 (c) The EDAX pattern of PSHS (75:25) crystal

### 5.4.2 EDAX of praseodymium samarium hydrogen selenite

The praseodymium samarium hydrogen selenite crystals are grown by the diffusion of 0.5M of $Pr(NO_3)_3$ and $Sm(NO_3)_3$ in different stoichiometric combinations. The EDAX of the crystals are taken as in the case of PNHS crystals. Fig.5.13 shows the EDAX pattern obtained for the crystals in different stoichiometries. The presence of Pr and Sm are evident from the characteristic $L_\alpha$ and $L_\beta$ peaks for these elements. The peak of the binding energy value 5.03 keV corresponds to the $L_\alpha$ line of Pr, the peaks at 5.634, 6.2 and 6.58 are corresponding to the $L_\alpha$, $L_{\beta1}$ and $L_{\beta2}$ peaks of Sm. The observed experimental data obtained are summarised in the table.5.23

**Table. 5.23 Summary of EDAX analysis of PSHS crystals**

| Expt. No. | Elements present in the mixed crystals | The ratio of the upper reactants (by volume) | The observed % of rare aearths |
|---|---|---|---|
| 1 | Pr, Sm | 25 : 75 | 25.302, 74.698 |
| 2 | Pr, Sm | 50 : 50 | 50.401, 49.599 |
| 3 | Pr, Sm | 75 : 25 | 75.212, 24.788 |

It is noteworthy that the percentage of Pr and Sm in the crystal is in accordance with the proportion of the corresponding rare earth solution in the supernatant solution. The presence of Pr and Sm in the PSHS crystal is established by the presence of $L_\alpha$ and $L_\beta$ peaks of Pr and $L_\alpha$, $L_{\beta1}$ and $L_{\beta2}$ peaks of Sm, which are matching well with the EDAX international chart . It is also noted that the increase in concentration of the Pr ions produce changes in the heights (area) of the $L_\alpha$ and $L_\beta$ peaks of Pr. The same effect is observed in the case of Sm also.

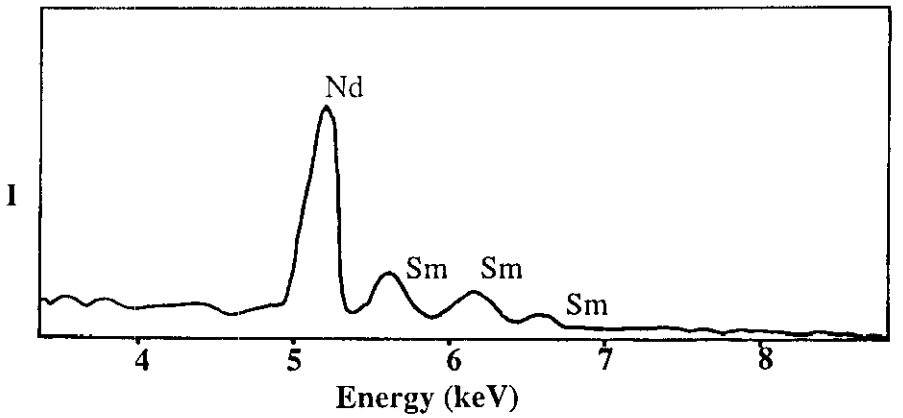


Fig. 5.14 (a) The EDAX pattern of NSHS (75:25) crystal

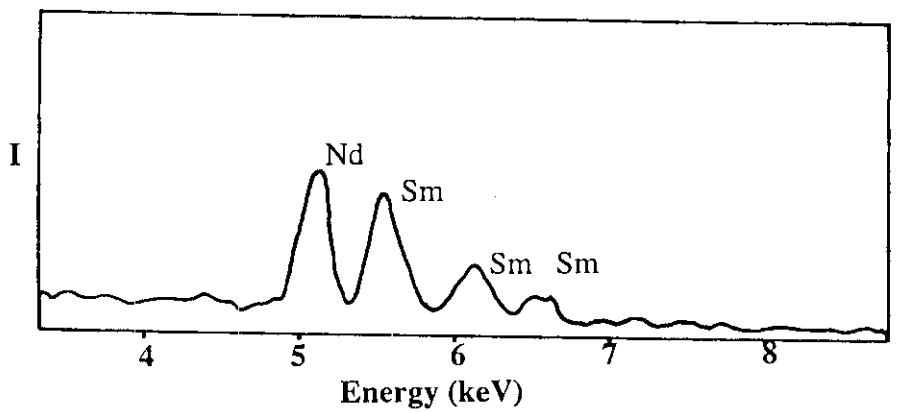


Fig. 5.14 (b) The EDAX pattern of NSHS (50:50) crystal

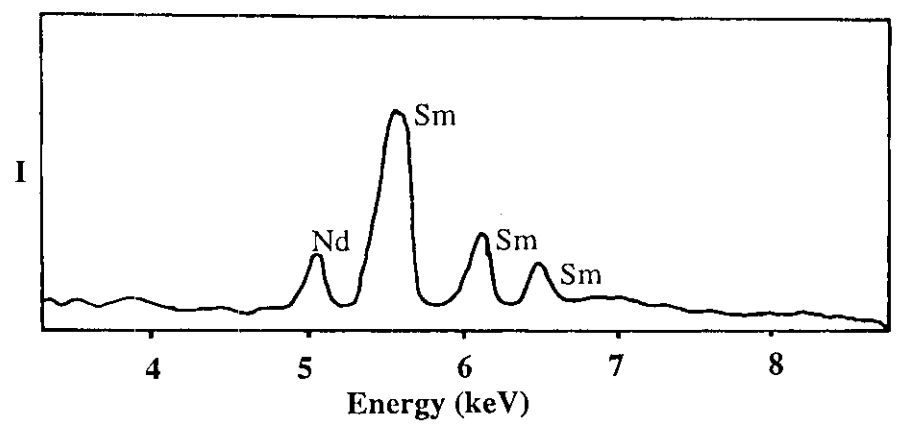


Fig. 5.14 (c) The EDAX pattern of NSHS (25:75) crystal

### 5.4.3 EDAX of neodymium samarium hydrogen selenite

The neodymium samarium hydrogen selenite crystals grown by the diffusion of different volumes in solution of 0.5M solutions of $Nd(NO_3)_3$ and $Sm(NO_3)_3$ through set gel containing anions. Fig 5.14 shows the measured EDAX pattern. The presence of Nd ions in the grown crystals are clear from the $L_\alpha$ peak of Nd corresponding to the binding energy value of 5.23 KeV. The peaks at binding energy values 5.64, 6.2 and 6.62 keV, correspond to $L_\alpha$, $L_{\beta 1}$ and $L_{\beta 2}$ peaks of samarium which confirm the presence of Sm. The presence of peaks at 5.23, 5.7 and 6.04 keV, correspond to the $L_\alpha$, $L_{\beta 1}$ and $L_{\beta 2}$ peaks of Nd. It is noteworthy that the heights (area) of the peaks increases with the increase in percentages of constituent rare earth ion present in the mixed crystals. The fig.5.14 shows the pattern obtained and the quantitative analysis are shown in table 5.24.

**Table. 5.24 Summary of EDAX analysis of NSHS crystals**

| Expt. No. | Elements present in the mixed crystals | The ratio of the upper reactants (by volume) | The observed % of rare earths |
|---|---|---|---|
| 1 | Nd, Sm | 25 : 75 | 24.123, 74.877 |
| 2 | Nd, Sm | 50 : 50 | 46.069, 53.931 |
| 3 | Nd, Sm | 75 : 25 | 73.820, 26.180 |

## 5.5 Thermal analysis

### 5.5.1 Thermogravimetric analysis (TGA)

Only a few cases of thermogravimetric studies on different selenite crystals or compounds[12,13,14] have been reported. The thermogravimetric measurements give a relation connecting the mean temperature and percentage loss of the mass of the sample[15]. It also throws light on the chemical equation of the compound or crystal. In this analysis the weight loss is recorded with time due to the dehydration and or decomposition of the sample. The change in weight is attributed to the creation of the physical and chemical bonds at elevated temperatures, which transforms the phase of the material. Thermogravimetry is ideally suited to study this unique sequence of the phase changes at higher temperature.

The thermal decomposition of all the rare earth hydrogen selenite crystals were examined thoroughly. The thermogram of rare earth mixed crystals show almost identical behaviour. The samples undergo successive decomposition of $H_2O$ and $SeO_2$ molecules. Table 5.25-5.27 gives the analytical data of the crystals. Fig.5.15 gives the TGA curves of all the mixed (PNHS, PSHS and NSHS) crystals .

The chemical formula of the mixed crystals are, $Pr_{1-x}Nd_x(HSeO_3)(SeO_3).2H_2O$, $Nd_{1-x}Sm_x(HSeO_3)(SeO_3).2H_2O$, $Pr_{1-x}Sm_x(HSeO_3)(SeO_3)\ 2H_2O$. Thermogravimetric and differential thermal analysis were performed by using SETRAM TGDTA92 in the atmosphere of argon and oxygen from $5^0C$ to $1200^0C$. Standard platinum crucibles were employed as sample holder and heating rate was $10^0C$/min and the sample weight was 100mg.

Thermal decomposition of PNHS, NSHS and PSHS was examined thoroughly and it occurred in six steps between $135^0C$ to $1200^0C$ depending on the constituent rare earth elements. It is worth noting that the thermal behaviour of these crystals are identical characterised by successive decomposition of $H_2O$ and $SeO_2$ molecules. The calculated and observed values after degradation tallied with the proposed molecular formula (tables 5.25-5.27). The functional groups were characterised with the IR absorption spectrum of the samples heated for different temperatures (fig.5.16). The observed result complement the TG&DTA data. Table gives the characteristic peaks of the functional groups present in the IR spectrum of the crystals.

**Table. 5. 25 Thermal degradation of PNHS crystals**

| DTA Temp. ($^0C$) | Range of Temp. T.G ($^0C$) | Observed % of Weight loss | Calculated % of Weight loss |
|---|---|---|---|
| 175 | 135-195 | 2.1 | 2.08 |
| 250 | 235-325 | 8.2 | 8.48 |
| *388 | 325-475 | 6.1 | 6.11 |
| 540 | 475-585 | 7.4 | 7.68 |
| 850 | 585-904 | 32 | 33.31 |
| 1182 | 904-1200 | 22 | 24.1 |

**Table. 5.26 Thermal degradation data of NSHS Crystals**

| DTA Temp. ($^0$C) | Range of Temp. T.G ($^0$C) | Observed % of Weight loss | Calculated % of Weight loss |
|---|---|---|---|
| 180 | 145-245 | 2.2 | 2.05 |
| 265 | 245-300 | 8.0 | 8.3 |
| *395 | 300-450 | 7.0 | 7.05 |
| 565 | 450-620 | 10.0 | 10.15 |
| 830 | 620-900 | 24.8 | 24.64 |
| 1150 | 900-1200 | 34.00 | 34.84 |

**Table. 5.27 Thermal degradation data of PSHS Crystals**

| DTA Temp. ($^0$C) | Range of Temp. T.G ($^0$C) | Observed % of Weight loss | Calculated % of Weight loss |
|---|---|---|---|
| 170 | 125-200 | 2.5 | 2.06 |
| 265 | 200-300 | 8.2 | 8.40 |
| *375 | 300-420 | 7.0 | 7.40 |
| 555 | 420-600 | 7.6 | 7.69 |
| 840 | 600-900 | 32 | 33 |
| 1160 | 900-1200 | 20.5 | 20 |

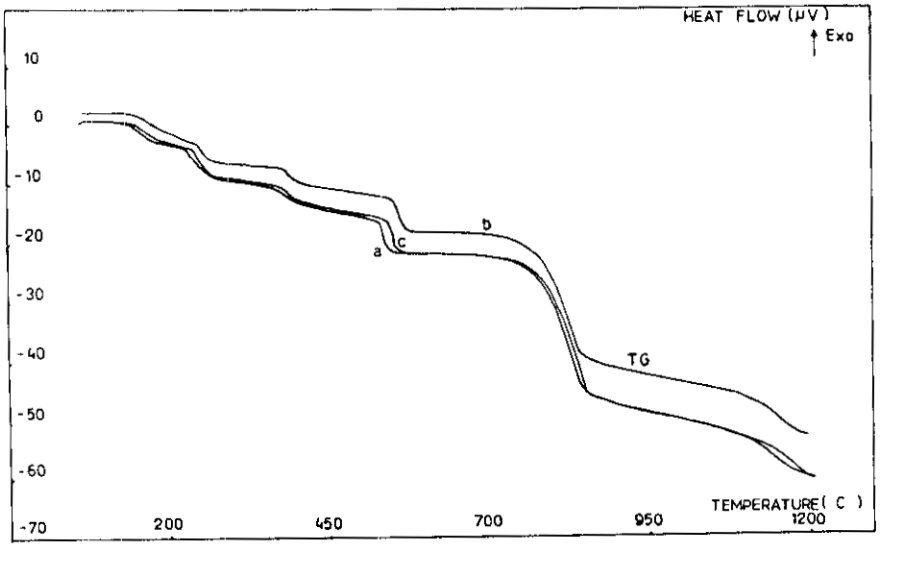


Fig. 5.15 Themogravimetric curve of mixed rare earth selenites
(a) PNHS crystal (b) NSHS crystal (c) PSHS crystal

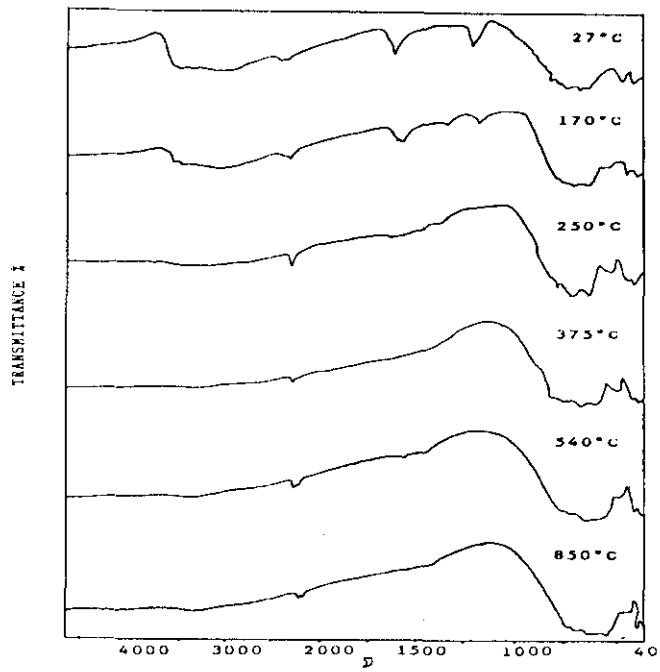


Fig. 5.16 FT-IR Spectra of rare earth hydrogen selenite (PNHS) crystal heated at different temperatures

(1) $27^0$ C (2) $170^0$ C (3) $250^0$ C (4) $375^0$ C (5) $550^0$ C (6) $900^0$ C

The thermal decomposition of all the stages can be depicted as

$2[RR_1(HSeO_3)(SeO_3).2H_2O] - 1H_2O \rightarrow RR_1Se_4O_{11}.4H_2O - 4H_2O \rightarrow RR_1Se_4O_{11} - 1/2SeO \rightarrow \frac{1}{2}[4RR_1Se_7O_{20}] - \frac{1}{2}SeO_2 \rightarrow RR_1Se_3O_9 - 2SeO_2 \rightarrow RR_1SeO_3 - 1SeO_2 \rightarrow RR_1O_3$

Where R and $R_1$ are the constituent rare earth elements.

The decomposition curves of PNHS, PSHS, NSHS are identical in nature and it is in good agreement with that single selenite crystals[16]. The proposed chemical formula and IR spectra of these crystals are matching with each other[16]. As in the case of rare earth oxalates[17], we propose that these crystals can be used as precursor for the preparation of the corresponding superconducting oxides.

### 5.5.2 The differential thermal analysis (DTA)

The DTA curves of all the mixed crystals (fig.5.17) show five endothermic peaks in accordance with the mass loss as shown in TG curve except for the decomposition of $RR_1SeO_{11}$, that is an exothermic peak (the temperature region showing * signs in the table. 5.25-5.27). This peak can be regarded as the elimination of $SeO_2$ and simultaneous crystallographic transformation.

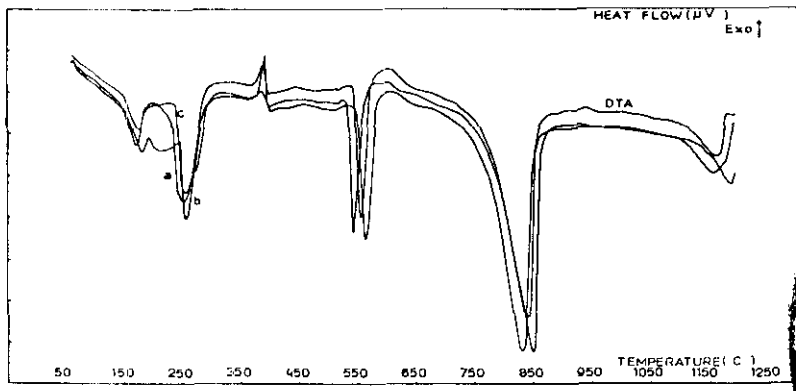


Fig. 5.17 DTA curve of mixed rare earth hydrogen selenites.
(a) PNHS crystal (b) NSHS crystal (c) PSHS crystal

## 5.6 Conclusion

The XRD analysis conclusively revealed the crystal class and gave the unit cell dimension. The only reference in the literature is of praseodymium hydrogen selenite. The reported data on unit cell dimension agree with the experimental data. Depending on the atomic dimension cell parameters show slight changes in the case of mixed crystals. The IR studies at different temperatures of the samples reveal the correctness of the calculated formula. The conclusion is again confirmed from the FT-IR spectrum. EDAX studies revealed the percentage of rare earth components in the crystal and UV-Visible absorption emission spectra correctly identified the presence of rare earth ions. The TG-DTA results corroborates and confirms the assumed chemical formula.

## References


[1] Edward Salisbury Dana., *'Textbook of mineralogy'* 4th ed. William E.Ford., Wiley Eastern Ltd. 1985

[2] Keith, R.E., Gilman, J., *Acta Metall* **8** (1960)

[3] Gilmann, J.J., Johnston, W.G., *J. Appl phys* **27** (1956)1018

[4] Walrafen, G. E., *J. Chem. Phys.* **36** (1962) 90

[5] Brian, G. Wbourne, *'Spectroscopic properties of rare earths'*, Interscience publishers, John Wiley and Sons, Inc, New York, 1965

[6] Asprey, L. B and Cunningham, B. B, Proc. *Inorg. Chem*, **2** (1960) 267

[7] Carnal, W.T., Fields, P.R and Rajnak, K, *J. Chem. Phys.* **49** (1968) 4424

[8] Cunningham, B. B, *Intro. Congr. Pur. Appl. Chem.* **17** (1959) 64

[9] Michal Malinowski., *J. Phys. Chem. Solids* **51** (1990) 59

[10] Carnal, W.T., Fields, P.R and Wybourne, B.G. *J. Chem. Phys.* **42** (1965) 3797

[11] Aumuller, G.C., *J. Phys. Chem. Solids* **55** (1994) 767

[12] Ionashiro,M., Melios, C. B., Ribeiro, C. A., Spiradili Crespi, M and I. Giolito, *Thermochim. Acta* **168** (1990) 223

[13] Barfiwala, U.A. and Ajaokar, V.R., *J. Thermal Analysis,* **44** (1995) 1463

[14] R. E Morris, J. A Hriljac and A. K Cheetam, *Acta Cryst.* **C 46** (1990) 2013

[15] Mahadeo., Nabar. A and Ajgaokar, V.R, *J. Less-Common metals.* **106** (1985) 211

[16] Castro,A., Enjalbert,R., M. de Pedro, and Trombe, J. C., *J. of Solid State Chem.* **112** (1994) 418

[17] Vickery, R. C. *'Analytical Chemistry of Rare Earths'* Pergamon Press, Oxford 1966